Multisensory Control of Hippocampal Spatiotemporal Selectivity

Pascal Ravassard,[1,2]* Ashley Kees,[1,3]* Bernard Willers,[1,2]* David Ho,[1,3] Daniel Aharoni,[1,2] Jesse Cushman,[1,2] Zahra M. Aghajan,[1,2] Mayank R. Mehta[1,2,3,4]†

The hippocampal cognitive map is thought to be driven by distal visual cues and self-motion cues. However, other sensory cues also influence place cells. Hence, we measured rat hippocampal activity in virtual reality (VR), where only distal visual and nonvestibular self-motion cues provided spatial information, and in the real world (RW). In VR, place cells showed robust spatial selectivity; however, only 20% were track active, compared with 45% in the RW. This indicates that distal visual and nonvestibular self-motion cues are sufficient to provide selectivity, but vestibular and other sensory cues present in RW are necessary to fully activate the place-cell population. In addition, bidirectional cells preferentially encoded distance along the track in VR, while encoding absolute position in RW. Taken together, these results suggest the differential contributions of these sensory cues in shaping the hippocampal population code. Theta frequency was reduced, and its speed dependence was abolished in VR, but phase precession was unaffected, constraining mechanisms governing both hippocampal theta oscillations and temporal coding. These results reveal cooperative and competitive interactions between sensory cues for control over hippocampal spatiotemporal selectivity and theta rhythm.

Spatial navigation and hippocampal activity are influenced by three broad categories of stimuli: distal visual cues (*1*, *2*); self-motion cues (*3*, *4*), e.g., proprioception, optic flow, and vestibular cues (*5*); and other sensory cues (*6*, *7*), e.g., olfaction (*6*, *8*), audition (*9*), and somatosensation (*10*). Although the cognitive map is thought to be primarily driven by distal visual and self-motion cues (*11*), their contributions are difficult to assess in the real world (RW). Hence, we developed a noninvasive virtual reality (VR) (fig. S3) for rats, where the vestibular and other sensory cues did not provide any spatial information. Consequently, we will refer only to proprioception and optic flow as "self-motion cues," and vestibular inputs will be treated separately. Place cells have been measured in VR in mice with their heads fixed (*12*, *13*) and are thought to be similar in VR and RW, but this has not been tested. We used tetrodes to measure neural activity from the dorsal CA1 of six rats while they ran in VR or RW environments consisting of a linear track in the center of a square room with distinct distal visual cues on each of the four walls (Fig. 1A). The visual scene was passively turned when rats reached the end of the virtual track. The distal visual cues were nearly identical in VR and RW, but rats' bodies were fixed in VR, which eliminated spatially informative other sensory cues and minimized both angular and linear vestibular inputs (fig. S4, see methods). Thus, the only spatially informative cues in VR during track running were distal visual and self-motion cues, as defined above. During recordings, rats ran consistently along the track and reliably slowed before reaching the track end in both VR and RW (Fig. 1B, see methods). Although their running speed was somewhat lower in VR than RW, their behavioral performance was similar.

Clear, spatially focused and directionally tuned place fields, commonly found in RW (Fig. 1C), were also found in VR (Fig. 1D) (*12*). Almost all track-active putative pyramidal cells had significant spatial information in VR (96%) and RW (99%). Thus, distal visual and self-motion cues are sufficient to generate the hippocampal rate code or cognitive map. We then examined whether the cognitive maps were similar in VR and RW.

We measured the activities of 2119 and 528 putative pyramidal neurons in the baseline sessions, conducted in a sleep box, preceding the VR and RW tasks respectively (see methods). Of these, 45.5% were track-active in RW. In contrast, only 20.4% were track-active in VR (Fig. 1E and fig. S5). The VR track-active cells had only slightly smaller mean firing rates (VR: 2.71 ± 0.08 Hz, $n = 432$, RW: 3.06 ± 0.12 Hz, $n = 240$, $P < 0.05$), which is likely due to lower running speed (*14*). Although the track-active cells were measured during locomotion, we also investigated the place-cell activation during periods of immobility at the goal locations, where a similar reduction to one-half of the proportion of goal-active cells in RW was seen in VR, with no significant change in firing rates (table S1 and Fig. 1E).

The firing rate maps of place cells were slightly less stable in VR (stability index 0.80 ± 0.01, $n = 432$) than RW (0.87 ± 0.01, $n = 240$). Hence, all subsequent comparisons were made across only the 392 and 227 track-active, stable cells (fig. S6, see methods) in VR and RW respectively. Place fields were 26% wider ($P < 10^{-10}$) in VR (55.8 ± 1.2 cm, $n = 482$) compared to RW (44.3 ± 1.4 cm, $n = 365$). As a result, spatial selectivity was 22% lower in VR (Fig. 1F, fig. S7, and table S1). Further, 90% (75%) of track-active cells had at least one place field in RW (VR), and place fields had comparable and significantly asymmetric shapes in both VR and RW such that the firing rates were higher at the end of a place field than at the beginning (table S1) (*12*, *15*, *16*).

We then investigated the directionality of place cells in VR. As in RW (*14*), the majority of place cells were directional, spiking mostly in one running direction (Fig. 1, C and D). In fact, the distributions of directionality index were identical (fig. S7 and table S1). But, bidirectional cells (40% in VR and 43% in RW), which had substantial activity along both running directions, showed different behavior in RW and VR (Fig. 2A). Bidirectional cells fired around the same absolute position on the track in both running directions in RW (Fig. 2A) (*6*, *17*), expressing a position code. In contrast, bidirectional cells in VR fired around the same distance from the start position in both running directions (Fig. 2A), indicative of a disto-code. The position code index (see methods) was significantly positive in RW but significantly negative in VR, indicating a position code in RW and its absence in VR (Fig. 2B). Exactly the opposite was true for the disto-code (Fig. 2C). Analysis of trials run at different speeds showed that spiking was more correlated with distance along the track than the duration of running, suggesting that it is distance run rather than time that determined these cells' activity (fig. S8).

To assess these results at the population level, we performed population vector overlap analysis (Fig. 2, D and E, and fig. S9; see methods). The population of bidirectional cells spiked around the same absolute position on the track in two movement directions in RW, indicated by a significant increase in population vector overlap along the −45° diagonal (Fig. 2D). There was no significant overlap along +45° (at the same distance along two directions) in RW. The opposite was true in VR (Fig. 2E), with significant overlap along +45° and no significant overlap along −45°. Thus the disto- and position codes were present at the population level in VR and RW respectively, but not vice versa.

Examination of the same cells recorded in both VR and RW revealed that their mean firing rates, spatial information, and directionality index were correlated between the environments, but the position of their place fields was unrelated (figs. S10 and S11). In the same bidirectional cells, the disto-code index was greater in VR than in RW, and the position code index was greater in RW than VR (fig. S12).

Having examined the rate-code, we investigated the temporal features (*12*, *16*, *18*–*20*) of place cells. The frequency of theta rhythm (see methods) in the local field potential (LFP) during locomotion was reduced in VR compared to RW (Fig. 3A). Despite this, VR cells showed clear phase precession, comparable to RW (Fig. 3, B and C). Indeed, across the ensemble of data, the LFP theta frequency within place fields was

[1]W. M. Keck Center for Neurophysics, Integrative Center for Learning and Memory, and Brain Research Institute, University of California, Los Angeles, Los Angeles, CA 90095, USA. [2]Department of Physics and Astronomy, University of California, Los Angeles, Los Angeles, CA 90095, USA. [3]Neuroscience Interdepartmental Program, University of California, Los Angeles, Los Angeles, CA 90095, USA. [4]Departments of Neurology and Neurobiology, University of California, Los Angeles, Los Angeles, CA 90095, USA.

*These authors contributed equally to this work.
†Corresponding author. E-mail: mayankmehta@ucla.edu

8.7% lower in VR compared to RW (Fig. 3D), yet there was no significant difference in the quality of phase precession between the two conditions (Fig. 3E). As a result, the frequency of theta modulation of spiking of place cells (*12*, *16*, *18*–*21*) was also significantly reduced in VR (fig. S13). Thus the frequency of theta rhythm is different in VR and RW, but it has no impact on the hippocampal temporal code.

Theta frequency was significantly lower in VR than RW at all running speeds (Fig. 4, A and B). Across the ensemble, theta frequency increased with running speed in RW but this was abolished in VR (Fig. 4B). We thus computed the speed dependence of theta frequency for each electrode within each session (see methods). Noisy but clear speed-dependent increase in theta frequency was found within single LFP data in RW (Fig. 4C), but not in VR (Fig. 4D). These calculations of the single cycle theta frequency could be influenced by noise, which could especially distort the low-amplitude theta and provide erroneous results. Hence, we restricted the analysis to only high-amplitude theta cycles (see methods). A large majority (85.4%) of LFPs in RW showed significant correlation between running speed and theta frequency but this was abolished in VR (Fig. 4E and figs. S14 and S15). In contrast, theta amplitude showed identical correlation with running speed in both conditions (Fig. 4F).

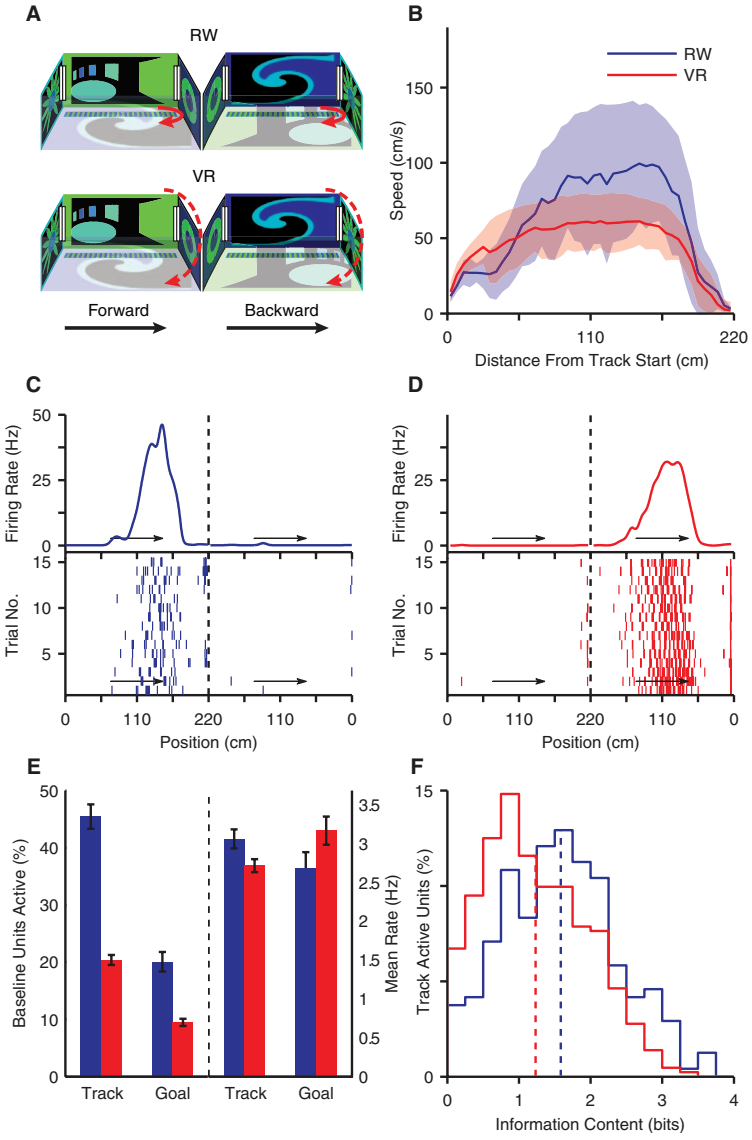

Fig. 1. Large reduction of track-active cells in VR without comparable reduction in firing rates. (**A**) Schematic of the task environment and distal visual cues in VR and RW. Rats turned themselves around in RW, whereas the scene was passively reversed in VR. (**B**) Running speed (means ± SD) of rats as a function of position on a 2.2-m-long linear track for RW (blue) and VR (red). Similar color scheme is used throughout. Although the rats were faster in RW, their behavior was similar, reliably reducing speed before reaching the end of the track (n = 49 sessions in RW, n = 128 sessions in VR). (**C**) Example of a directional, stable place cell recorded in RW with firing rate (top), and raster plot (bottom). Arrows indicate running direction. (**D**) A similar place cell recorded in VR. (**E**) Comparison of activation ratio and firing rates of active cells on track (RW: 45.5%, 3.06 ± 0.12 Hz; VR: 20.4%, 2.71 ± 0.08 Hz) and at goal (RW: 20.1%, 2.68 ± 0.20 Hz; VR: 9.5%, 3.16 ± 0.18 Hz). (**F**) Spatial information content across 432 track-active cells in VR (1.23 ± 0.03 bits, n = 432) was significantly lower (22%, $P < 10^{-7}$) than in 240 RW cells (1.58 ± 0.05 bits, n = 240).

The key findings were qualitatively true within each animal. In particular, within each animal the disto (position) index was positive (negative) in VR, and negative (positive) in RW, a substantially greater fraction of cells were active in RW than VR and theta frequency was greater in RW than VR. Further, control experiments show that the disto-code was not driven by salient reward, indicating cues in the environment (figs. S16 and S17); was present in both passive and active turning protocols (fig. S18); and was consistent between slow and fast trials in VR (fig. S19).

These results reveal several important aspects of the sensory mechanisms governing hippocampal rate and temporal codes. Comparable levels of spatial selectivity and firing rates of track-active cells in VR and RW, as well as comparable strength of temporal code, all show that a robust cognitive map can indeed be formed with only distal visual and self-motion cues providing spatial information. However, these cues alone do not determine the location of place fields between VR and RW, as shown by the differences in ratemaps of the same cells.

The VR and RW environments had similar dimensions and nearly identical distal visual cues, and the rats' behavior was similar in the two conditions. Thus, these factors are unlikely to cause the observed differences in place cell activity between VR and RW. Several other factors could potentially contribute, in particular, the absence of spatial information in vestibular and other sensory cues, or conflicts of other sensory cues with distal visual or self-motion cues in VR. One potential consequence of conflicting cues could be reference frame switching (between virtual and real space) occurring randomly along the track, resulting in loss of spatial selectivity in VR. The overwhelming presence of significant spatial information in cells recorded in VR argues against this possibility. Instead, these results suggest that additional sensory cues present in RW are necessary for the activation of a subpopulation of CA1 place cells, such that their removal reduces the activation of place cells without altering the firing rates of active cells. In VR, spatial information is provided by only distal visual and self-motion cues, which likely change more slowly than spatially informative proximal cues, such as odors along the track in RW. This could make place fields wider in VR and therefore reduce their information content.

The switch in coding observed in the bidirectional cell population is analogous to a previous report of different hippocampal cell response types (*4*), which implies either distinct classes of principal cells or alternate responses from the

same cells depending on the task. The latter seems to be more likely in our data because comparisons between VR and RW show that the same hippocampal cell can acquire a different form of representation given a different subset of inputs. We cannot rule out the possibility that higher-order cognitive processes may influence the place cell code; however, it is likely that sensory inputs play a key role in our results. Similar levels of directional tuning in VR and RW suggest that distal visual cues, which are the only cues that differ along two movement directions on the track in VR, are sufficient to generate directional firing on a linear track. Vestibular inputs are not required for generating spatially selective, directional place cells, in contrast to previous lesion-based studies (*5*). The vestibular cues are present and identical along two movement directions in RW; therefore, their presence, not their absence, should contribute to a disto-code (figs. S20 and S21). Bidirectional cells in RW exhibit position code (*17*), which is enhanced by the addition of odors and textures (*6*). These points suggest proximal cues in RW are the most likely to generate the position code. Bidirectional cells in VR exhibit disto-code and are likely governed by self-motion cues, which are the only cues that are similar along the two movement directions. Finally, we hypothesize that other sensory cues present in RW have a veto power over self-motion cues in determining the bidirectional code.

Although disto-code has been reported on a single-unit level in RW (*3*, *22*), we do not see significant disto-code in the RW population. Further, the effect of self-motion cues on the hippocampal population code and the suggested competitive interaction between self-motion and other sensory cues are surprising. Such competitive effects between different sensory modalities may be driven by inhibitory mechanisms across multimodal inputs, as seen recently in the primary visual cortex (*23*), which suggests their broader applicability. We hypothesize that some other sensory cues reach CA1 via the lateral entorhinal cortex (LEC), because LEC neurons respond to local cues such as objects (*24*), whereas distal visual and self-motion cues reach CA1 via the medial entorhinal cortex (MEC) grid cells, which are influenced by these cues (*25*). Consistently, both LEC and MEC project directly and indirectly to CA1 and differentially modulate CA1 activity in vivo during sleep (*26*) and engage local inhibition (*27*). The competitive interactions governing the behavior of bidirectional cells in VR and RW may therefore be the result of inhibitory interactions between the LEC and MEC pathways.

Theta frequency was significantly reduced in VR, corroborating earlier results that vestibular inputs contribute to theta frequency (*28*), and its speed dependence was abolished. On the other hand, theta power had similar speed dependence in VR and RW, which suggested that theta power is largely governed by distal visual and self-motion cues. Despite the large changes in theta frequency and its speed dependence, phase precession was intact in VR (*12*), and its quality was identical in RW and VR, which indicated that distal visual and self-motion cues are sufficient to generate a robust temporal code. Our results place restrictions on theories of phase precession that depend on the precise value of theta frequency or its speed dependence (*18*, *29*–*31*). Instead, they favor alternative mechanisms that are insensitive to these phenomena (*15*, *16*, *19*) and that apply equally to networks with diverse connectivity patterns, such as the entorhinal cortex and CA1, and, hence, do not require recurrent excitatory connections (*15*, *16*). These results thus provide insight about how distinct sensory cues cooperate and compete to influence theta rhythm and hippocampal spatiotemporal selectivity.

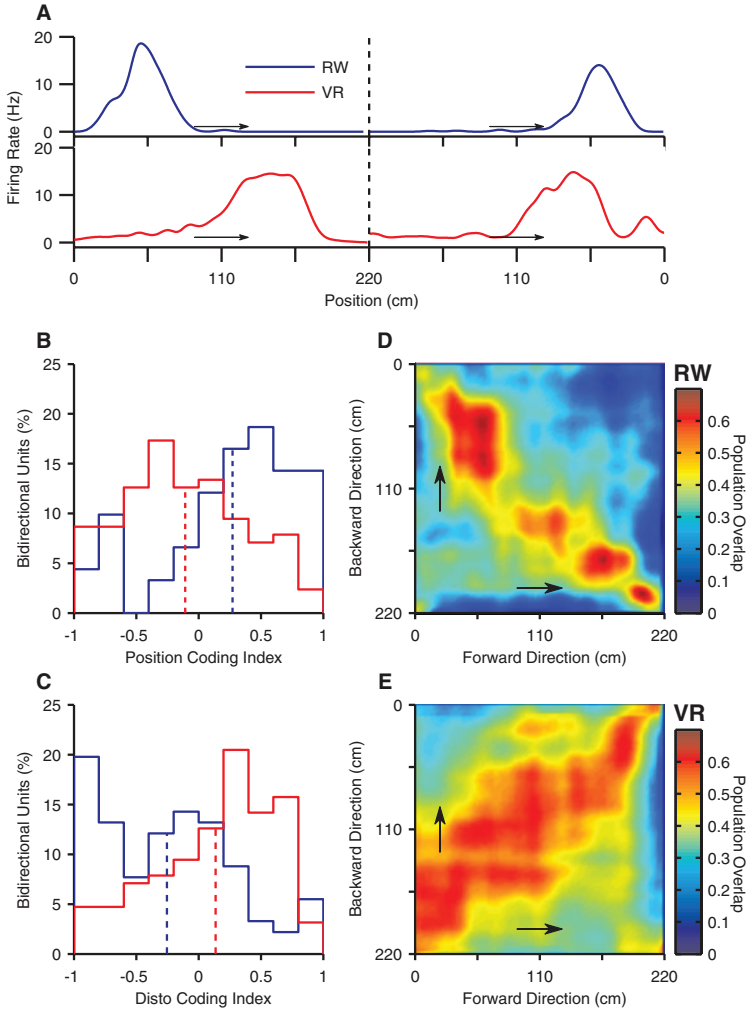

Fig. 2. Bidirectional place cells exhibit position code in RW but disto-code in VR. (**A**) Firing rate maps along both running directions for bidirectional cells in RW (top) and VR (bottom). (Top) A position-coding cell firing at the same position in both running directions. (Bottom) A disto-coding cell firing at the same distance in both directions. (**B**) Position code index is significantly positive in RW (0.27 ± 0.05, $P < 10^{-6}$, $n = 91$) but significantly negative in VR (-0.11 ± 0.04, $P < 0.05$, $n = 127$). (**C**) The disto-code index is significantly positive in VR (0.14 ± 0.04, $P < 0.001$, $n = 127$) but significantly negative in RW (-0.25 ± 0.06, $P < 10^{-4}$, $n = 91$). The position code index is significantly greater in RW than VR ($P < 10^{-7}$) whereas disto-code index is significantly greater in VR ($P < 10^{-6}$). (**D**) Similarity of the population of 91 bidirectional cells in RW between two movement directions was computed using the population vector overlap (see methods). Each colored pixel shows the vector overlap between two positions in opposite running directions. Note the clear increase in overlap along the −45° diagonal indicating spiking at the same position. (**E**) As in (D), for the population of 127 bidirectional cells in VR. Note the clear increase in overlap along the +45° diagonal, indicating spiking at the same distance in both running directions.

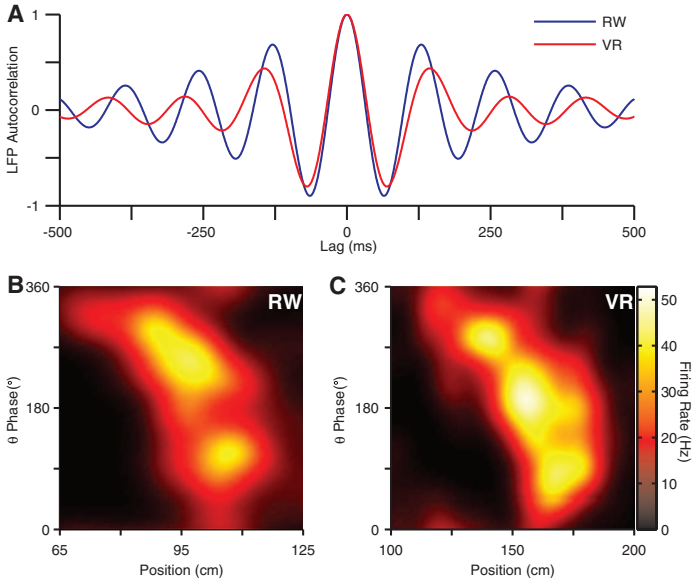

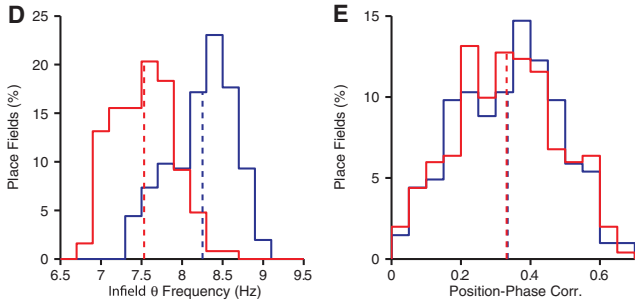

Fig. 3. Reduced theta frequency in VR without significant change in phase precession. (**A**) Autocorrelation function of sample hippocampal LFPs in RW and VR showing significant increase in theta period in VR. Both LFPs are recorded from same electrode on the same day. (**B**) Representative place field in RW showing clear phase precession. (**C**) Representative place field in VR showing clear phase precession. (**D**) In-field theta frequency of place fields in VR (7.53 ± 0.02 Hz, n = 251) was significantly less (8.7%, $P < 10^{-10}$, n = 204) than that of place fields in RW (8.25 ± 0.03 Hz, n = 204). (**E**) Quality of phase precession, measured by position-phase linear-circular correlation, in RW (0.33 ± 0.01) was not significantly different (P = 0.8) from precession in VR (0.33 ± 0.01).

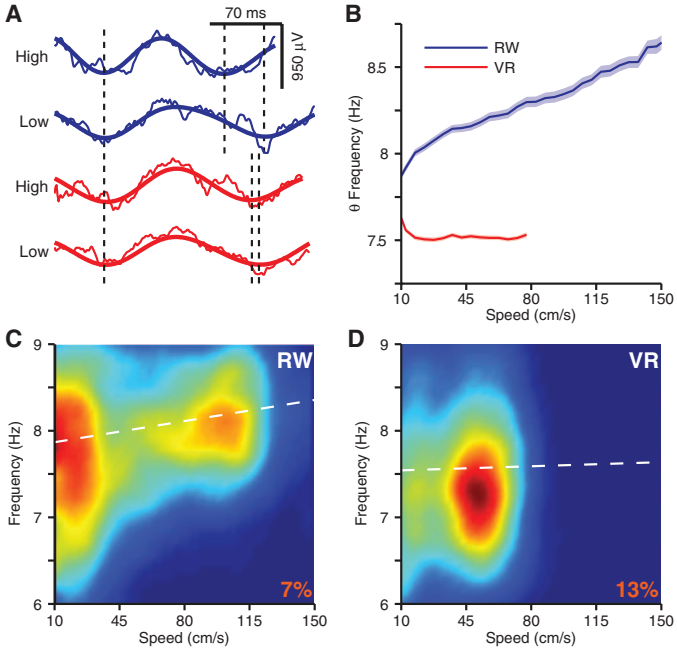

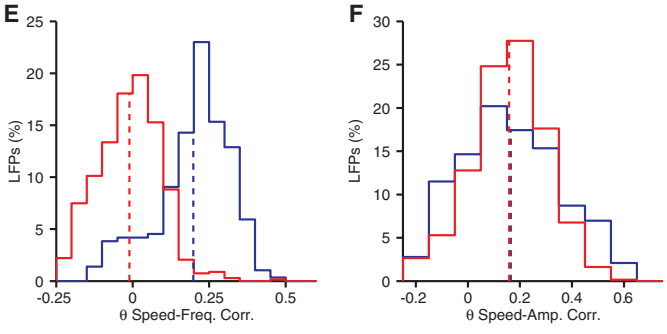

Fig. 4. Absence of theta-frequency speed dependence in VR. (**A**) Sample theta cycles during high (>50 cm/s) and low (<10 cm/s) running speed in RW and VR from the same electrode seen in Fig. 3A. Bold lines are filtered between 4 and 12 Hz, narrow lines are unfiltered traces (see fig. S15). (**B**) Population average (mean ± SEM) speed dependence of theta frequency from 287 LFPs in RW and 681 LFPs in VR. (**C**) Density map of individual theta-cycle frequencies and corresponding speeds from a single LFP in RW (correlation = 0.13, $P < 10^{-10}$). (**D**) As in C, for the same electrode in VR on the same day (correlation = 0.01, P = 0.48). (**E**) The population of LFPs in RW shows significant correlation between theta frequency and speed (0.21 ± 0.01, $P < 10^{-10}$), whereas the population of LFPs in VR shows no significant correlation (−0.01 ± 0.01, $P < 0.01$). (**F**) Theta cycle amplitude is similarly (P = 0.8) correlated with speed in both RW (0.16 ± 0.01) and VR (0.16 ± 0.01).

References and Notes

1. J. O'Keefe, J. Dostrovsky, *Brain Res.* **34**, 171 (1971).
2. R. U. Muller, J. L. Kubie, *J. Neurosci.* **7**, 1951 (1987).
3. K. M. Gothard, W. E. Skaggs, B. L. McNaughton, *J. Neurosci.* **16**, 8027 (1996).
4. E. Pastalkova, V. Itskov, A. Amarasingham, G. Buzsáki, *Science* **321**, 1322 (2008).
5. R. W. Stackman, A. S. Clark, J. S. Taube, *Hippocampus* **12**, 291 (2002).
6. F. P. Battaglia, G. R. Sutherland, B. L. McNaughton, *J. Neurosci.* **24**, 4541 (2004).
7. E. Save, L. Nerad, B. Poucet, *Hippocampus* **10**, 64 (2000).
8. E. R. Wood, P. A. Dudchenko, H. Eichenbaum, *Nature* **397**, 613 (1999).
9. P. M. Itskov, E. Vinnik, C. Honey, J. W. H. Schnupp, M. E. Diamond, *J. Neurophysiol.* **107**, 1822 (2012).
10. B. J. Young, G. D. Fox, H. Eichenbaum, *J. Neurosci.* **14**, 6553 (1994).
11. J. O'Keefe, L. Nadel, *The Hippocampus as a Cognitive Map* (Clarendon Press, Oxford, 1978).
12. C. D. Harvey, F. Collman, D. A. Dombeck, D. W. Tank, *Nature* **461**, 941 (2009).
13. D. A. Dombeck, C. D. Harvey, L. Tian, L. L. Looger, D. W. Tank, *Nat. Neurosci.* **13**, 1433 (2010).
14. B. L. McNaughton, C. A. Barnes, J. O'Keefe, *Exp. Brain Res.* **52**, 41 (1983).
15. M. R. Mehta, M. C. Quirk, M. A. Wilson, *Neuron* **25**, 707 (2000).
16. M. R. Mehta, A. K. Lee, M. A. Wilson, *Nature* **417**, 741 (2002).
17. E. Resnik, J. M. McFarland, R. Sprengel, B. Sakmann, M. R. Mehta, *J. Neurosci.* **32**, 8952 (2012).
18. J. O'Keefe, M. L. Recce, *Hippocampus* **3**, 317 (1993).
19. M. V. Tsodyks, W. E. Skaggs, T. J. Sejnowski, B. L. McNaughton, *Hippocampus* **6**, 271 (1996).
20. T. Hafting, M. Fyhn, T. Bonnevie, M. B. Moser, E. I. Moser, *Nature* **453**, 1248 (2008).
21. C. Geisler, D. Robbe, M. Zugaro, A. Sirota, G. Buzsáki, *Proc. Natl. Acad. Sci. U.S.A.* **104**, 8149 (2007).
22. K. Mizuseki, S. Royer, K. Diba, G. Buzsáki, *Hippocampus* **22**, 1659 (2012).
23. G. Iurilli *et al.*, *Neuron* **73**, 814 (2012).
24. S. S. Deshmukh, J. J. Knierim, *Front. Behav. Neurosci.* **5**, 69 (2011).
25. T. Hafting, M. Fyhn, S. Molden, M. B. Moser, E. I. Moser, *Nature* **436**, 801 (2005).
26. T. T. G. Hahn, J. M. McFarland, S. Berberich, B. Sakmann, M. R. Mehta, *Nat. Neurosci.* **15**, 1531 (2012).
27. T. T. Hahn, B. Sakmann, M. R. Mehta, *Nat. Neurosci.* **9**, 1359 (2006).

28. N. A. Russell, A. Horii, P. F. Smith, C. L. Darlington, D. K. Bilkey, *J. Neurophysiol.* **96**, 4 (2006).
29. N. Burgess, *Hippocampus* **18**, 1157 (2008).
30. M. E. Hasselmo, L. M. Giocomo, E. A. Zilli, *Hippocampus* **17**, 1252 (2007).
31. H. T. Blair, A. C. Welday, K. Zhang, *J. Neurosci.* **27**, 3211 (2007).

Acknowledgments: This work was supported by the NSF Career award and grants from NIH 5R01MH092925-02 and the W. M. Keck foundation. These findings were presented as two abstracts and posters at the Society for Neuroscience Meeting entitled: P. Ravassard, B. Willers, A. L. Kees, D. Ho, D. Aharoni, M. R. Mehta, "Directional tuning of place cells in rats performing a virtual landmark navigation task," *Soc. Neurosci. Abs.* no. 812.05 (2012); and A. Kees, B. Willers, P.M. Ravassard, D. Ho, D. Aharoni, M. R. Mehta, "Hippocampal rate and temporal codes in a virtual visual navigation task," *Soc. Neurosci. Abs.* no. 812.07 (2012). We thank L. Acharya, Z. Chen, and J. Moore for technical help. Author contributions: P.R., A.K., D.H., and J.C. performed data collection; B.W. and D.A.A. developed the virtual reality system; B.W. and Z.M.A. performed analysis; P.R., A.K., B.W., and Z.M.A. wrote the manuscript; P.R., A.K., B.W., D.H., D.A.A., and J.C. designed the experiment; and M.R.M. participated in all of the above.

Supplementary Materials
www.sciencemag.org/cgi/content/full/science.1232655/DC1
Materials and Methods
Figs. S1 to S21
Table S1
References

12 November 2012; accepted 16 April 2013
Published online 2 May 2013;
10.1126/science.1232655

Subangstrom Resolution X-Ray Structure Details Aquaporin-Water Interactions

Urszula Kosinska Eriksson,[1]† Gerhard Fischer,[1]*† Rosmarie Friemann,[1] Giray Enkavi,[2] Emad Tajkhorshid,[2]‡ Richard Neutze[1]‡

Aquaporins are membrane channels that facilitate the flow of water across biological membranes. Two conserved regions are central for selective function: the dual asparagine-proline-alanine (NPA) aquaporin signature motif and the aromatic and arginine selectivity filter (SF). Here, we present the crystal structure of a yeast aquaporin at 0.88 angstrom resolution. We visualize the H-bond donor interactions of the NPA motif's asparagine residues to passing water molecules; observe a polarized water-water H-bond configuration within the channel; assign the tautomeric states of the SF histidine and arginine residues; and observe four SF water positions too closely spaced to be simultaneously occupied. Strongly correlated movements break the connectivity of SF waters to other water molecules within the channel and prevent proton transport via a Grotthuss mechanism.

Aquaporins are water transport facilitators found in all kingdoms of life (*1*). They are primarily responsible for water homeostasis within living cells, although a subset of aquaporins also facilitates the flow of other small polar molecules, such as glycerol or urea. As with any membrane transport facilitator, aquaporins have evolved to be highly selective for their transported substrate without binding water so strongly that transport is inhibited. In addition to excluding hydroxide (OH^-) and hydronium (H_3O^+) ions, aquaporins must also prevent proton transport via a Grotthuss mechanism (*2*, *3*) in which protons are rapidly exchanged between hydrogen bonded water molecules.

Crystal structures of bacterial (*4*, *5*), archael (*6*), yeast (*7*), plasmodium (*8*), plant (*9*), mammalian (*10*–*12*), and human (*13*–*15*) aquaporins have established that these channels contain six transmembrane α helices and associate as homotetramers. A seventh pseudo-transmembrane helix is formed by loops B and E, which fold as aligned half-helices that insert from opposite sides of the membrane and place the conserved dual asparagine-proline-alanine (NPA) signature motif near the center of the water pore (Fig. 1). Transport specificity is defined by the aromatic and arginine selectivity filter (SF) (*16*, *17*), which is located near the extracellular pore entrance and forms the narrowest portion of the channel.

Several models accounting for the ability of aquaporins to impede the passage of protons have emerged from structural arguments (*13*), molecular dynamics (MD) investigation of water structure and dynamics (*17*, *18*), and computational studies characterizing the energetics associated with explicit transfer of protons across the channel (*19*, *20*). These studies assert different microscopic mechanisms for excluding protons, including electrostatic repulsion (*19*, *21*–*23*), configurational barriers (*17*), and desolvation penalties (*24*), and they consistently report the NPA region, where the macrodipoles of the two half-helices formed by loops B and E focus a positive electrostatic potential, as the main barrier against proton transport (*17*–*24*). This creates an electrostatic barrier to proton transport (*21*) and orients the water molecule's dipole moment near the NPA motif, such that the order of oxygen and hydrogen atoms do not support proton exchange via a Grotthuss mechanism (*17*, *18*). Although intuitively appealing, this picture does not explain why mutations within the NPA motifs that diminish this positive electrostatic barrier facilitate the transport of sodium ions, but not protons (*25*, *26*); nor is it evident why mutations within the SF can allow the channel to conduct protons (*27*, *28*).

To further examine the underlying mechanism of facilitated, selective water transport, we optimized crystals of Aqy1 (*7*), the sole aquaporin of *Pichia pastoris*, and determined its crystal structure to 0.88 Å resolution (*29*), recovering *R*-factor and R_{free} values of 10.3% and 10.7%, respectively (table S1). The electron density associated with the dual-NPA–aquaporin signature motif is illustrated in Fig. 2. At subangstrom resolution, the conformations of the two NPA asparagine residues (Asn^{112} and Asn^{224}) are uniquely assigned because the $2mF_{obs} - DF_{calc}$ electron density is delocalized across the carbon-oxygen double bond of these side chains (Fig. 2, A and B, blue mesh), whereas that for the side-chain nitrogen atom is more localized: *m* is the figure of merit, and *D* is estimated from coordinate errors. Electron density associated with Glu^{51} (fully delocalized) and Gln^{137} (partially delocalized) highlights how delocalized density can be distinguished at this resolution (fig. S1). It is noteworthy that residual $mF_{obs} - DF_{calc}$ difference electron density, from a hydrogen omit map (Fig. 2, A and B, green mesh), reveals electron clouds associated with all four proton-donor interactions of the Nδ atoms of the dual-NPA asparagine residues. H-bond donor interactions of Asn^{224}:Nδ to water molecule 6 (Wat6) (peak maximum 0.42 e/Å^3) (Fig. 2A) and to the carbonyl oxygen of Leu^{111}, as well as H-bond donor interactions of Asn^{112}:Nδ to Wat7 (peak maximum 0.48 e/Å^3) (Fig. 2B) and to the carbonyl oxygen of Leu^{223}, are all resolved. These observations confirm that H-bond donor interactions from the NPA motifs constrain the orientation of passing water molecules (*13*, *17*, *18*). No modeled water has H-bond interactions with both NPA asparagines, as is often depicted (*13*, *17*, *19*, *22*, *23*), and a water molecule at this position cannot be the critical ingredient preventing Grotthuss proton transport.

MD simulations have predicted that water molecules adopt a bipolar orientation in the two halves of the channel, such that proton-donor interactions systematically point away from the NPA region, which disfavors Grotthuss proton exchange (*13*, *17*, *18*). In the cytoplasmic half-channel, residual $mF_{obs} - DF_{calc}$ electron density

[1]Department of Chemistry and Molecular Biology, University of Gothenburg, Box 462, S-40530 Göteborg, Sweden. [2]Department of Biochemistry, College of Medicine, Center for Biophysics and Computational Biology, and Beckman Institute for Advanced Science and Technology, University of Illinois, Urbana, IL 61802, USA.
*Present address: Department of Biochemistry, University of Cambridge, CB2 1GA Cambridge, UK.
†These authors contributed equally to this work.
‡Corresponding author. E-mail: richard.neutze@chem.gu.se (R.N.); emad@life.illinois.edu (E.T.)

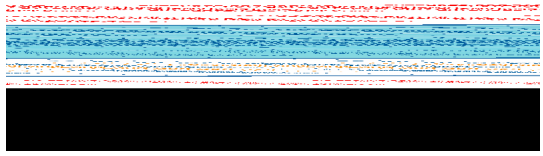

Multisensory Control of Hippocampal Spatiotemporal Selectivity
Pascal Ravassard, Ashley Kees, Bernard Willers, David Ho, Daniel Aharoni, Jesse Cushman, Zahra M. Aghajan and Mayank R. Mehta (May 2, 2013)
Science **340** (6138), 1342-1346. [doi: 10.1126/science.1232655] originally published online May 2, 2013

Editor's Summary

A Sense of Place

Hippocampal place cells are believed to be mainly governed by visual and self-motion cues. However, the contribution of sensory cues such as smells, sounds, and textures, etc., is difficult to eliminate. In virtual reality, these cues will not provide any information about the animals' position. **Ravassard *et al.*** (p. 1342, published online 2 May) developed a virtual-reality system as immersive and close to the real world as possible and compared place cells in rats running in this apparatus and in the real world. Twice as many neurons were active in a real-world situation compared to virtual reality. While place cells in the real world encoded position, place cells in a virtual world encoded distance.

Science (print ISSN 0036-8075; online ISSN 1095-9203) is published weekly, except the last week in December, by the American Association for the Advancement of Science, 1200 New York Avenue NW, Washington, DC 20005.